Extended wavelength and enhanced sensitivity of PbS colloidal quantum dots/Bi₂Te₃ photodetector by band alignment engineering

Lijing Yu [a,b,c], Pin Tian [b,c], Libin Tang [a,b,c,*], Qun Hao [a,*], Kar Seng Teng [d,*], Hefu Zhong [e], Wenbin Zuo [b,c], Yulong Ji [b], Hongfu Li [b], Zhihua Li [b], Qi Ma [b], Min Yang [b], Lianjie Yu [b]

[a] The Laboratory of Photonics Information Technology, Ministry of Industry and Information Technology, School of Optics and Photonics, Beijing Institute of Technology, Beijing 100081, China
[b] Kunming Institute of Physics, Kunming 650223, China
[c] Yunnan Key Laboratory of Advanced Photoelectric Materials & Devices, Kunming 650223, China
[d] Department of Electronic and Electrical Engineering, Swansea University, Bay Campus, Fabian Way, Swansea SA1 8EN, United Kingdom
[e] School of Materials and Energy, Yunnan University, Kunming 650500, China

HIGHLIGHTS

- Wavelength extension of the photodetector is realized by the synergistic effect of PbS colloidal quantum dots and Bi₂Te₃.
- The photodetector demonstrates a broadband response from ultraviolet (UV) to short-wave infrared (SWIR).
- High responsivity of ~161 A/W and detectivity of ~3.2 × 10¹³ Jones at 1050 nm are obtained by band alignment engineering.

GRAPHICAL ABSTRACT
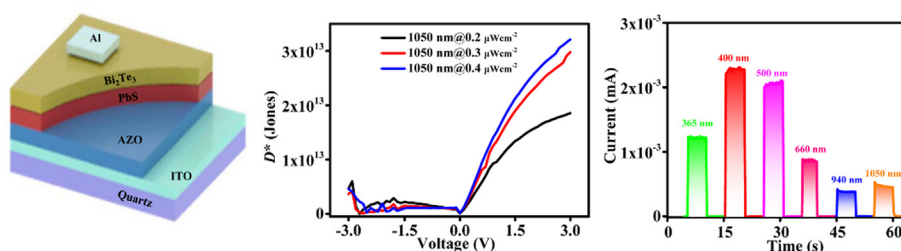
ABSTRACT

The tunable band gap of PbS colloidal quantum dots (CQDs) from ultraviolet (UV) to short-wave infrared (SWIR) bands provides many potential applications in optoelectronics. However, synthesis of large-sized CQDs that exhibit good stability and sensitivity for extended wavelength still remains a technological challenge. In this paper, a novel broadband photodetector based on small size PbS CQDs (with exciton absorption peak at 927 nm) and Bi₂Te₃ (with wide spectral sensitivity and high absorption) was developed and studied. The device, which comprised of ITO/AZO/PbS CQDs/Bi₂Te₃/Al, provided an excellent band alignment that facilitated charge dissociation and transmission hence improving the device sensitivity. Furthermore, wavelength extension was also realized through the synergistic effect of these materials, thus demonstrating broadband photodetection with high sensitivity. The heterostructure photodetector demonstrated good performance in the visible and near infrared ranges, especially at a wavelength of 1050 nm exhibiting a high responsivity (R) and detectivity (D^*) of 161 A/W and 3.2×10^{13} Jones, respectively. In addition, the device exhibited excellent stability and reversibility after one month of storage without any encapsulation. This work lays a good foundation for the construction of the next generation of highly sensitive broadband CQDs photodetectors.

---

* Corresponding authors at: The Laboratory of Photonics Information Technology, Ministry of Industry and Information Technology, School of Optics and Photonics, Beijing Institute of Technology, Beijing 100081, China (L. Tang).

E-mail addresses: scitang@163.com (L. Tang), qhao@bit.edu.cn (Q. Hao), k.s.teng@swansea.ac.uk (K.S. Teng).

1. Introduction

Broadband photodetector is of great research interests due to their potential applications in optical communication, medical

diagnosis and environmental monitoring [1,2], etc. In order to extend the operating wavelength and improve the performance of the device, many device structures have been designed and developed, for example, photodetector exhibiting high sensitivity and wide spectrum can be realized by combining several different functional materials (such as two-dimensional materials) [3]. However, its application is limited due to the complex production process and the use of expensive equipment (such as chemical vapor deposition and so on), hence rendering them commercially unviable [4]. CQDs have attracted much research interests due to their unique properties, such as adjustable band gap, quantum confinement effect and solution processability, [5] etc. PbS CQD is the most widely studied CQD. It has a high molar absorption coefficient ($\approx 10^6$ M^{-1} cm^{-1}) and a wide adjustable band gap range (0.6–1.6 eV)[6], providing the possibility for low-cost broadband photoelectric applications from UV to SWIR. So far, it has been used in photoelectric detection [7], solar cells [8], and light-emitting diodes [9], etc.

Band gap of the quantum dots can be tuned by adjusting its size, structure and shape due to the quantum confinement effect [10]. For example, an increase in the quantum dot size would lead to weakening of the confinement, hence resulting in the redshift of the absorption spectrum (e.g., a larger dot size would result in significant redshift). In order to synthesize large-sized CQDs, higher growth temperature and longer growth duration are usually required [11]. As uncontrollable nucleation process and Ostwald ripening happened during the growth of the quantum dots, a prolonged growth duration can result in high defect density and poor dispersion [12,13] that have detrimental effects on the optical properties of the synthesized quantum dots. Therefore, it has been difficult to synthesize PbS CQDs with size of up to $\sim$ 3 μm [14].

Stability of the quantum dots is important to its application. The performance of the quantum dots can degrade due to oxidation, especially for PbX (X = S, Se, Te) quantum dots. The oxidation of PbS quantum dots is greatly affected by its surface properties, which are related to its crystal structure. PbX is a semiconductor with rock-salt cubic structure, of which [111] and [100] planes are the main crystal planes. The proportion of [100] and [111] facets on the CQDs surface plays a vital role in the overall stability of the material. Small-sized PbX nanoparticles usually have an octahedral shape with a higher ratio of [111] to [100] facets. As the size of quantum dots increases, the shape of the dots first evolves into truncated octahedrons and then into cuboctahedron, which causes the proportion of [100] facets to increase. As ligands preferentially bind to the [111] facets of PbX quantum dots, the higher proportion of [100] facets would reduce the ligand coverage hence lowering the inoxidizability of the quantum dots [15,16]. Therefore, large-sized PbS quantum dots oxidize easily and are difficult to synthesize. Broadening the response band by increasing the size of quantum dots remains a technological challenge to produce device that exhibits good and stable performances. To date, most methods to improve the performance of CQDs photodetectors have been focused mainly on enhancing carrier mobility but they did not result in significant improvement in device performance (e.g., responsivity was less than 1 AW^{-1}). The combination of CQDs with topological materials has demonstrated moderate improvement in the device performance [17], which attributed to the high mobility and unique surface states of the topological materials (such as Bi_2Te_3).

In this work, a novel broadband photodetector based on small-sized PbS CQDs/Bi_2Te_3 heterostructure was fabricated by spin coating and magnetron sputtering techniques. The photoelectric properties of UV–visible to near-infrared (365, 400, 500, 660, 940 and 1050 nm) broadband photodetectors have been studied in detail. The device exhibits a maximum responsivity and detectivity of 161 A/W and 3.2 × 10^{13} Jones, respectively, at a wavelength of 1050 nm. In addition, the device demonstrates excellent stability after one month of storage without packaging. The mechanisms of enhanced light response and wavelength extension of the PbS CQDs/Bi_2Te_3 heterostructure are discussed.

2. Experimental section

2.1. Materials

Indium tin oxide (ITO) grown on quartz substrate was obtained from Beijing Jinji Aomeng Technology Co. Ltd. PbS CQDs were synthesized by thermal injection as previously reported by Hines Ma et al [18]. A mixture, consisting of 1.2 g of PbO, 4 mL of oleic acid (OA) and 20 mL of octadecene (ODE), was heated to 100 °C and subsequently increased to 130 °C to form lead oleate, which was rapidly injected into the sulfur source. The flask was then cooled to room temperature in a cold bath. N-octane was purchased from Tianjin Zhiyuan Chemical Reagent Co. Ltd. The as-prepared PbS CQDs were dissolved in an n-octane solvent with a concentration of 30 mg/mL·NH_3·H_2O, H_2O_2 and methanol were obtained from Tianjin Fengchuan Chemical Reagent Co. Ltd. Tetrabutyl-ammonium iodide (TBAI) was obtained from Shanghai Titan Scientific Co. Ltd. Sputtering targets, such as Bi_2Te_3 (99.99 %), Aluminum-doped zinc oxide (AZO) (99.99 %) and Al (99.99 %), were purchased from Zhongnuo Advanced Material (Beijing) Technology Co. Ltd. The dispersed quantum dots were stored in a vacuum chamber for future use. All chemicals were used without further purification.

2.2. Fabrication of photodetector

The ITO substrate was cleaned by chemical bath in NH_3·H_2O: H_2O_2: H_2O (1:1:3) mixed solution for 30 min, rinsed with deionized water, blown dry with nitrogen and then transferred into the magnetron sputtering chamber. AZO functional layer was deposited under a pressure of 0.6 Pa and sputtering power of 100 W, and the growth duration was 1 h. Using a layer-by-layer (LBL) method [19], PbS CQDs was spin coated on AZO layer at 2500 rpm and TBAI ligand exchange was then performed for 60 s. This spin coating process was repeated eight times to form a layer of PbS CQDs film. After spin coating of the PbS CQDs, the Bi_2Te_3 film was deposited using magnetron sputtering under a pressure of 0.6 Pa and power of 200 W, and the growth duration was 1 s. Finally, aluminum electrode was deposited using physical vapor deposition (PVD) technique on to a pre-masked surface of the Bi_2Te_3 film. The effective photosensitive area of the device was 1.0 mm^2.

2.3. Characterization

Transmission electron microscopy (TEM), high-resolution transmission electron microscopy (HRTEM) and fast Fourier transform (FFT) characterizations were performed using a high-resolution transmission microscope (JEM-2100) operating at 200 kV. The phase structures of the materials were characterized by X-ray diffractometer (XRD) (Rigaku D/Max-RA) with Cu radiation source. The optical properties of the materials were studied using an ultraviolet–visible spectrophotometer (UV–VIS-NIR 3600). Fourier transform infrared (FTIR) spectra were acquired using a Bruker Tensor spectrometer. Raman spectroscopy was performed using a Raman microscope with an argon-ion laser at an excitation wavelength of 514.5 nm. X-ray photoelectron spectroscopy (XPS) (PHI Versa Probe II) was used to study the chemical bonds and elemental composition of the materials. The cross-sectional image of the device was obtained by scanning electron microscope (SEM, FEI

Quanta 200). *C-V* characteristics of the device were analyzed by the semiconductor device analyzer (Keysight B1500A).

To characterize the device performance, LEDs with different wavelengths (365, 400, 500, 660, 940 and 1050 nm) were used as light sources. The LEDs were driven by a signal generator (Agilent 33210A) and the test results were collected via a digital source meter (Keithley 2400). The light intensity of LEDs was calibrated using silicon optical power meter (FZ400).

3. Results and discussion

3.1. Characterization of PbS CQDs

Fig. 1(a) shows TEM, HRTEM and FFT (inset) images of the synthesized PbS CQDs with size of ~ 3 nm and exhibit good monodispersity. According to the FFT pattern, PbS CQDs have excellent crystallinity. Lattice fringes correspond to $(1\,1\,1)$ and $(2\,0\,0)$ lattice planes of the PbS CQDs can be observed from the HRTEM image, hence indicating a high crystallinity of the nanomaterials. Surface topography of the spin-coated PbS CQDs film was characterized with a profilometer in the range of 417×417 μm^2 (as shown in Fig. 1(b)), and the measured surface roughness (SA) of the film is ~ 0.6 nm. The results show good uniformity of the PbS CQDs film, which is critical to the formation of high-quality film by spin-coating. Fig. 1(c) shows the X-ray diffraction (XRD) pattern of PbS CQDs, and all peaks are conformed to the PbS standard PDF card (JCPDS# 02-1431). Fig. 1(d) shows the absorption spectrum of PbS CQDs, which reveals strong absorption in UV-NIR (1000 nm) range, thus indicating that the PbS CQDs are potential candidate materials for the preparation of UV-NIR photodetectors. The absorption peak of the first exciton of the PbS CQDs is located at 927 nm. According to Moreels equation [20], the size of PbS CQDs is ~ 3 nm, which is consistent with the TEM results. Fig. 1 (e) shows the Tauc diagram (obtained from Fig. 1(d)) and is used to determine the band gap of PbS CQDs. The calculated band gap

of PbS nanocrystals is 1.24 eV using the Tauc relationship as described below [21]:

$$\alpha(hv) = A(hv - E_g)^{1/2} \tag{1}$$

where A is the absorption coefficient (cm^{-1}), hv is the photon energy, α is a constant, and E_g is the optical band gap.

The surface of PbS CQDs synthesized by heat injection method was coated with long chain organics, such as oleic acid (OA). In order to improve the charge transfer efficiency at the surface of quantum dots, there is a need to replace these long chain ligands with short chain ligands. Typically, short chain ligands, such as 3-mercaptopropionic acid (MPA) or ethane dithiol (EDT) are used [22]. Since PbS CQD films treated with TBAI demonstrate high charge mobility and good stability in air [23,24], TBAI is selected for short chain ligand exchange in this work. Organic ligand coated at the surface of quantum dots often contain functional groups, such as carbon–carbon double bond, carboxyl group, hydroxyl group and carbonyl group. The existence of these groups can be determined by Fourier infrared transform (FTIR) spectrometer, which is used to investigate the vibration of different bonds from these functional groups [25]. After TBAI ligand exchange, the surface of PbS CQDs was characterized by FTIR spectroscopy to determine whether oleic acid is completely replaced by short-chain ligands, as shown in Fig. 1(f). Comparing the FTIR spectra of as-synthesized PbS CQDs with those after ligand exchange, the CH$_2$ stretching peaks (i.e., 2852 cm^{-1} and 2920 cm^{-1}) disappear after ligand exchange hence suggesting that the oleic acid ligands are completely replaced.

3.2. Characterization of Bi$_2$Te$_3$ film

The preparation of Bi$_2$Te$_3$ films by magnetron sputtering is depicted in Fig. 2(a). Bi$_2$Te$_3$ film was grown at sputtering power of 200 W, sputtering pressure of 5 Pa, gas flow of 60 standard cubic centimeters per minute (sccm), and sputtering duration of 1 s. Dur-
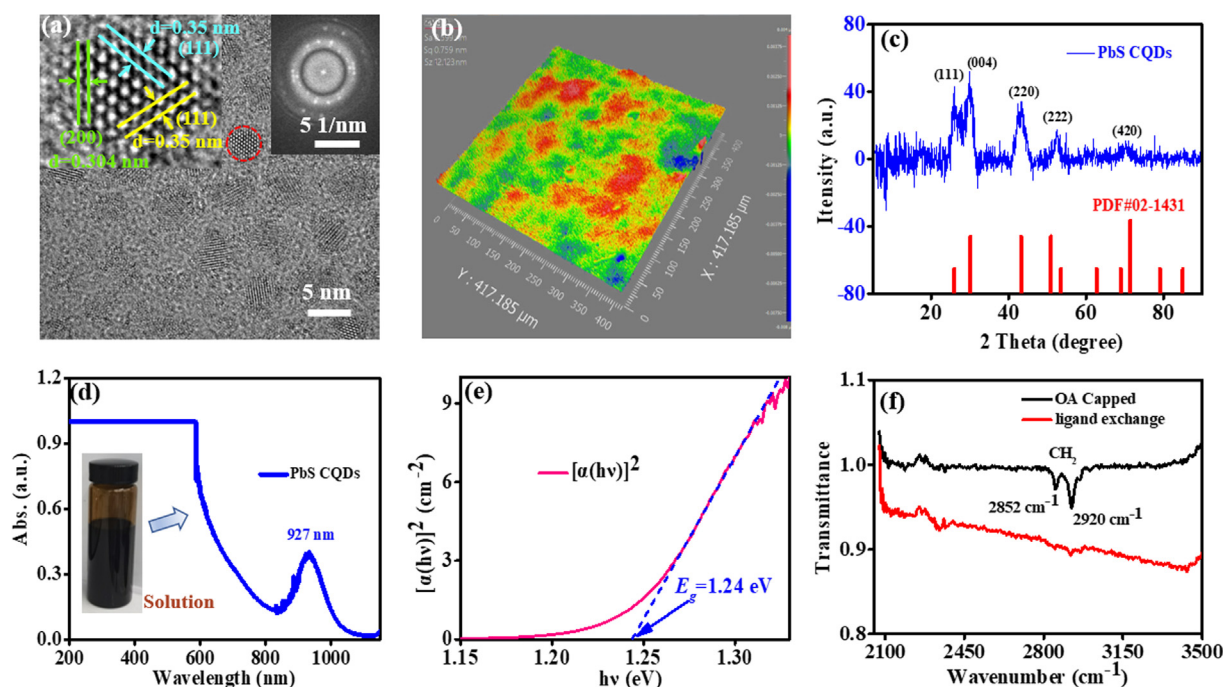

Fig. 1. Structural characterization of PbS CQDs. (a) TEM image of PbS CQDs (Inset: HRTEM and FFT images). (b) Surface topography of PbS CQDs film characterized by profilometry. (c) XRD pattern of PbS CQDs film. (d) UV–vis absorption spectrum of PbS CQDs. (e) Plot of α^2 versus photon energy (hv) of PbS CQDs film. (f) FTIR spectra of PbS CQDs film capped with oleic acid (black) and TBAI ligand (red). (For interpretation of the references to colour in this figure legend, the reader is referred to the web version of this article.)
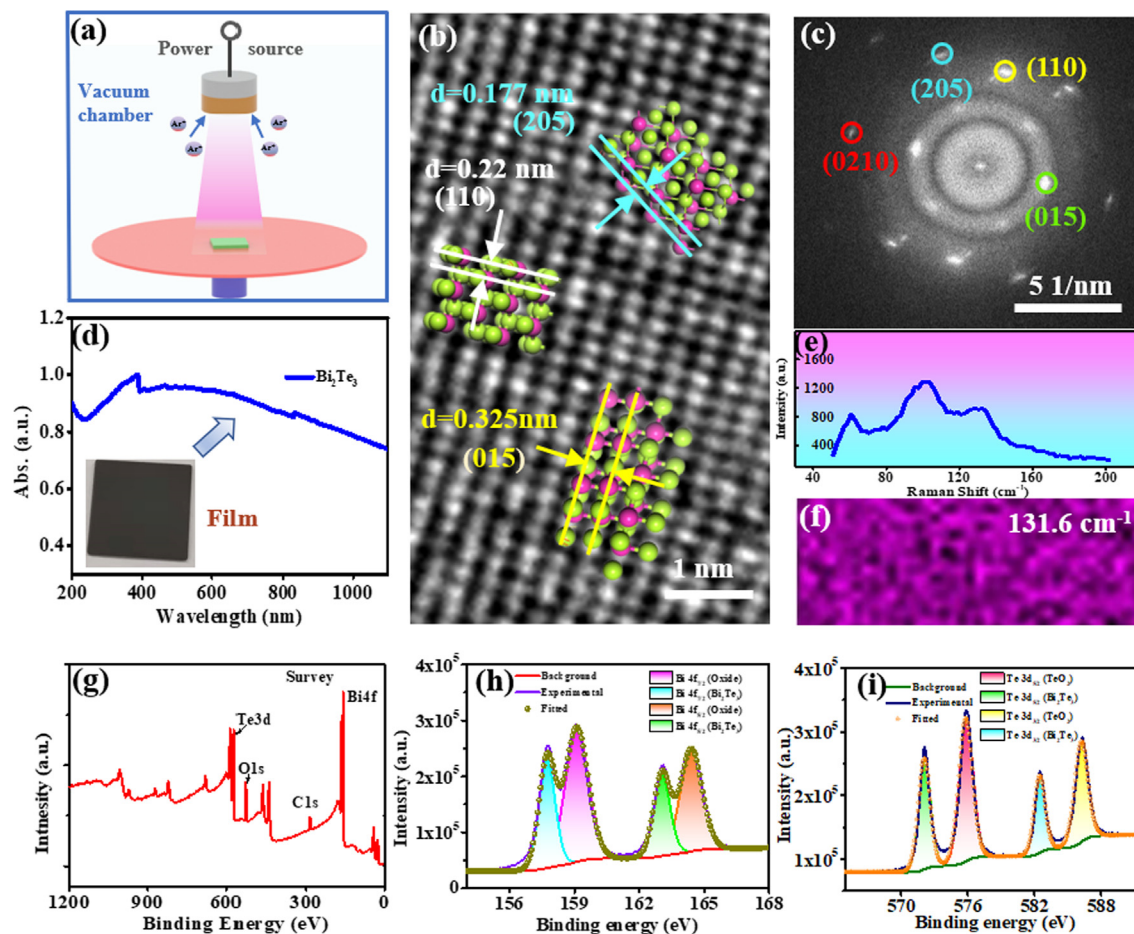
Fig. 2. Characterization of the Bi_2Te_3 film. (a) Schematic diagram depicting the preparation of Bi_2Te_3 film by magnetron sputtering. (b) HRTEM image and lattice structure (inset) of Bi_2Te_3 film. (c) FFT pattern of Bi_2Te_3 film. (d) UV–vis absorption spectrum of Bi_2Te_3 film. (e) Raman spectrum of Bi_2Te_3 film. (f) Raman mapping of Bi_2Te_3 film at 131 cm^{-1}. (g) XPS survey scan of Bi_2Te_3 film. (h) XPS spectrum of Bi 4f core level. (i) XPS spectrum of Te 3d core level.

ing sputtering, argon gas (Ar_2) is ionized to argon ion (Ar^+) and then accelerated to the Bi_2Te_3 target under an electric field. These argon ions bombard the surface of the target with high energy resulting in the sputtering of the target material onto the substrate. Fig. 2 (b) shows the HRTEM image of the deposited Bi_2Te_3 film. It can be seen that the Bi_2Te_3 film prepared by magnetron sputtering exhibits good crystallinity quality even without any annealing treatment. The HRTEM image of Bi_2Te_3 film reveals three different crystal faces with spacing of 0.177, 0.22 and 0.325 nm, corresponding to (205), (110) and (015) lattice planes, respectively. The observed lattice structures correspond to the theoretical lattice structures as shown in the insets of Fig. 2 (b). Fig. 2(c) shows the fast Fourier Transform (FFT) image of Bi_2Te_3 film, and the corresponding indices of crystal plane from Fig. 2(b) are marked on the image.

Bi_2Te_3 is a quintuple structure. Among the fifteen vibrational modes of Bi_2Te_3, the optical modes that can be detected by Raman spectroscopy are A_{1g}, E_g, E_u and A_{1u}. Among them, E_g originates from in-plane vibration of the five-layer structure, A_g is from out-of-plane vibration, and A_{1u} is caused by the defects of the quintuple structure [26]. The Raman spectrum of Bi_2Te_3 is shown in Fig. 2(e). It consists of three Raman peaks at 61.1, 101.1 and 131.6 cm^{-1}, which correspond to A_{1g}^1, E_g^2 and A_{1g}^2 of Bi_2Te_3, respectively. It is worth noting that A_{1u} peak is not observed in the spectrum, thus suggesting that the prepared Bi_2Te_3 film has a relatively low defect concentration. Fig. 3(f) shows the Raman mapping of the film at 131.6 cm^{-1} indicating the formation of a uniform film.

The chemical bond and surface oxidation state in Bi_2Te_3 film were studied by XPS. Fig. 2(g) shows the XPS survey spectrum of the film. Elements of Bi and Te, as well as O and C are observed in the spectrum. The presence of O 1s peak indicate surface oxidation of the film. The Bi 4f core level peak consists of doublet peaks, namely Bi $4f_{7/2}$ and Bi $4f_{5/2}$ at the binding energies of 157.7 eV and 163 eV, respectively, as shown in Fig. 2(h). Similarly, the core level peak of Te 3d also consists of doublet peaks (as shown in Fig. 2(i)), namely Te $3d_{5/2}$ and Te $3d_{3/2}$ at the binding energies of 572.2 eV and 582.4 eV, respectively. All the doublet peaks are deconvoluted into two components, such as the main and oxide-related peaks. The fitted Bi 4f and Te 3d core level peaks indicate that Bi_2Te_3 phase is formed [27]. The other four peaks at relatively higher binding energy (i.e., 159 and 164.3 eV of Bi 4f, and 575.9 and 586.2 eV of Te 3d) correspond to oxidation states and represent surface oxides at the Bi_2Te_3 film.

3.3. Characterization of photodetector

Fig. 3(a) shows the device structure of the photodetector, which comprises of ITO/AZO/PbS CQDs layer/Bi_2Te_3 /Al. Cross-sectional SEM image of the device is shown in Fig. 3(b). The layers (from top to bottom) are Al, Bi_2Te_3, PbS CQDs, AZO and ITO, with thickness of ∼ 90, 6, 172, 210 and 254 nm, respectively. An obvious boundary between the different materials can be seen from the SEM image, hence suggesting good interfaces are formed, which is favorable for fast transport of carriers.
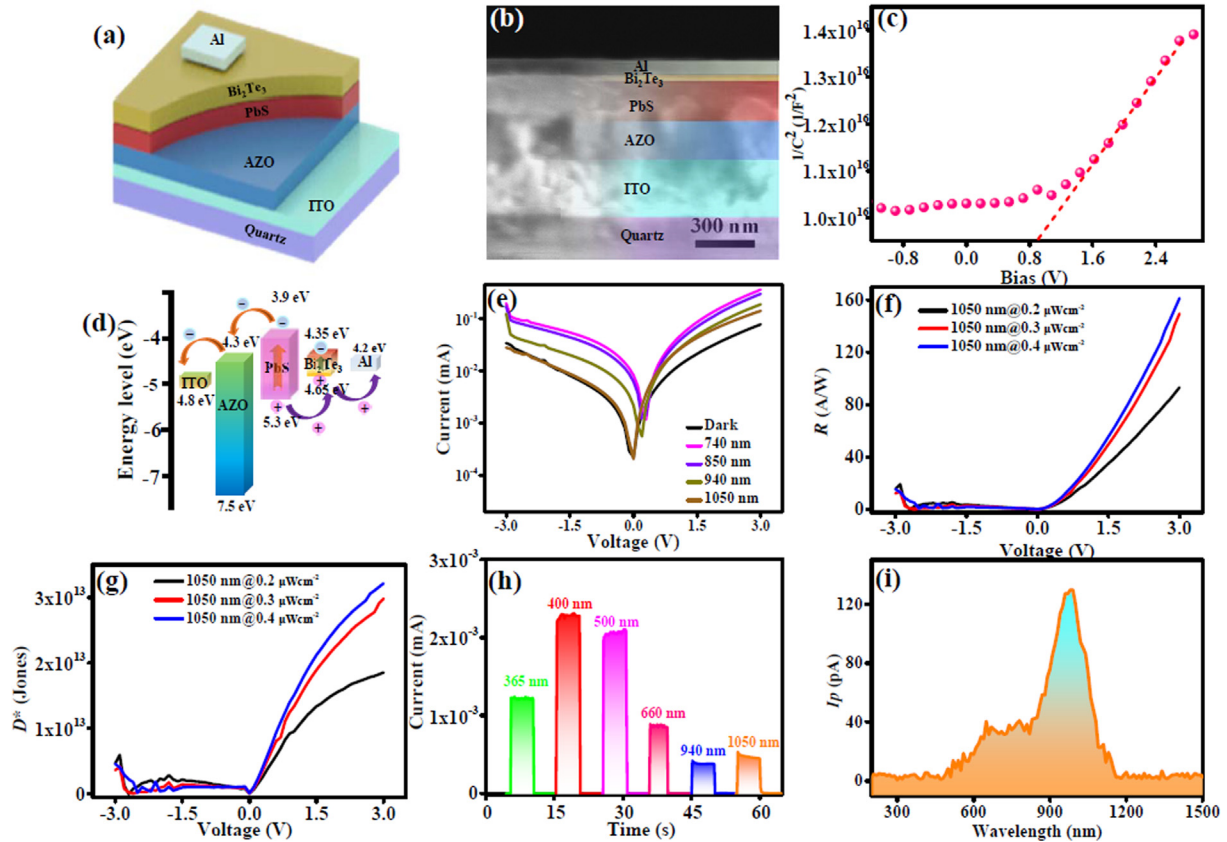
Fig. 3. (a) Schematic diagram illustrating the device structure. (b) Cross-sectional SEM image of the photodetector. (c) C–V characteristic of the photodetector. (d) Energy band diagram of the device. (e) I-V measurements under dark and different light wavelengths (740, 850, 940 and 1050 nm). (f) Plot of responsivity (R). (g) Plot of detectivity (D*). (h) Photoresponse under different light wavelengths (365, 400, 500, 660, 940 and 1050 nm). (i) Spectral response of the photodetector.

Capacitance-voltage (C-V) measurement is an effective method to study the doping concentration and barrier width of a p-n junction. Fig. 3(c) shows a $1/C^2$-V plot of the device. It is assumed that the depletion zone is entirely within the PbS CQD layer. In this case, the following formulas are used for analysis [28]:

$$\frac{1}{C^2} = \frac{2}{q\varepsilon_s}\frac{(\Phi - V)}{N_a} \qquad (2)$$

$$W = \sqrt{\frac{2\varepsilon_s(\Phi - V)}{qN_a}} \qquad (3)$$

where q is the electron charge, Φ is the built-in potential, Na is the doping concentration, and ε_s is the effective dielectric constant of CQD film. Using formula (1) and Fig. 3(c), Φ has a value of ∼ 0.9 V. Taking ε_s = 15 [29], the calculated values of Na and depletion width (W) of the device are 2.99×10^{16} cm^{-3} and 228 nm, respectively. As the thickness of the PbS CQD film is ∼ 172 nm (from the SEM image), this suggests that the depletion width of the device cover the entire CQD layer.

Fig. 3(d) shows the energy band diagram of the photodetector. Since the surface state density of the topological insulator (TI) Bi$_2$-Te$_3$ is much less than that of its bulk, the main focus is on the bulk state of Bi$_2$Te$_3$. According to the energy level position in the band diagram, the conduction band of AZO is lower than PbS CQDs, while the work function of ITO is lower than the conduction band of AZO, therefore there is no barrier to hinder the transport of electrons. The valence band of Bi$_2$Te$_3$ is higher than that of PbS CQDs, and the work function of Al is higher than that of Bi$_2$Te$_3$, which is conducive to the rapid transfer of holes.

Performance of the photodetector was studied using different wavelengths of incident light at room temperature. Fig. 3(e) shows that the optical response of the photodetector under 740, 850, 940 and 1050 nm wavelengths of incident light. Responsivity (R) and detectivity (D*) can be calculated using the following equations:

$$R = \frac{J_L - J_D}{P_{opt}} \qquad (4)$$

$$D^* = \frac{R}{(2qJ_D)^{1/2}} \qquad (5)$$

where J_L is the current density under incident light, J_D is the dark current density, P_{opt} is the optical power density, and q is the unit charge. The device exhibits high responsivity (R) and detectivity (D*) under illumination of 1050 nm light source at different power densities as shown in Fig. 3(f) and 3(g), respectively. An increase in both R and D* of the device is evident as the power density of the incident light increases. The photodetector has a maximum R and D* of 161 A/W and 3.2×10^{13} Jones, respectively. Compared with other PbS CQDs based photodetectors (Table 1), the device from this work exhibits excellent performance. Fig. 3(h) shows the transient response of the device under illumination at different wavelengths (365, 400, 500, 660, 940 and 1050 nm). Fig. 3(i) shows the spectral response of the device, which is beyond the absorption range of quantum dots. Even after one month of storage without packaging, the photodetector still demonstrates stable optical response at 740, 850, 940 and 1050 nm as shown in Fig. S1(a). According to the results in Fig. S1(b) and S1(c), there is no degradation in the responsivity (R) and detectivity (D*) of the device at 1050 nm. In addition, the time-dependent response of the

Table 1
Comparison the photoelectric properties with other PbS CQDs based photodetectors.

Materials	Excitation Wavelength (nm)	Responsivity (A/W)	Detectivity (Jones)	Ref.
PbS/ Bi_2Te_3	927	161	3.2×10^{13}	This work
PbS/graphene	1200	8×10^3	10^9	[30]
PbS/MoS$_2$	635	6×10^5	5×10^{11}	[31]
PbS/SnS$_2$	970	10^6	2.2×10^{12}	[32]
PbS/Si	1236	0.4	1.5×10^{11}	[33]
PbS / WSe$_2$	970	2×10^5	$\sim 10^{13}$	[34]

incident light at 365 nm (UV), 740 nm (visible) and 1050 nm (near infrared) are shown in Fig. S1(d)-(f), the results show that the device demonstrate good stability during repeated measurements and has a broad response from ultraviolet to near-infrared.

Many researchers have studied the relationship between the absorption spectrum of quantum dots and the response of the photoelectric device. For example, Keke Qiao [35] et al. fabricated a PbS CQDs based photodetector, which performance was attributed to the first excitonic absorption peak of the nanomaterial at 980 nm, and reported that the photocurrent dropped sharply to a level similar to that of dark current once the incident light exceeded its absorption range. Therefore, it can be concluded that the quantum dots with 927 nm exciton absorption peak would not result in an optical response at 1050 nm, and the excellent performance of the device achieved at 1050 nm must be due to the combination with Bi_2Te_3 material in this work.

The observed enhancement in performance and wavelength extension of the PbS CQDs/Bi_2Te_3 heterostructure photodetector can be explained as follows. The photosensitive layer absorbs photons resulting in the generation of excitons (i.e., hole-electron pairs). The holes are rapidly transferred from Bi_2Te_3 to Al electrode, while the electrons are transferred from AZO to ITO electrode. The rapid separation and extraction of carriers lead to the effective conversion of incident light to photocurrent, thus improving the performance of the device [36]. This transmission mechanism would explain the high responsivity of the device. In addition, a reasonably design of hybrid quantum dots/Bi_2Te_3 device can realize a high-performance CQDs photodetector through the internal gain phenomenon due to the large gap in carrier mobility between Bi_2Te_3 and quantum dots [37,38].

The photodetector consists of two active parts, namely the PbS CQDs and Bi_2Te_3 material. If the wavelength of incident light is within the absorption range of PbS CQDs, such as 927 nm, the PbS CQDs would play a dominant role because of its larger thickness producing stronger absorbance. If the wavelength of incident light is beyond the absorption range of PbS CQDs but within the absorption range of Bi_2Te_3, such as 1050 nm, Bi_2Te_3 would play a dominant role instead. The Bi_2Te_3 acts as a functional layer as well as broadens the absorption spectrum of the active layer of Bi_2Te_3/ PbS CQDs to 1050 nm by introducing an extra absorption peak at the near infrared (1050 nm) leading to strong absorption and broadband response.

4. Conclusion

In this work, a hybrid structure of AZO/Bi_2Te_3/PbS CQDs was designed and fabricated for use as photodetector, which exhibits excellent performance and wavelength extension. Compared with PbS CQDs photodetector, the synergistic action of PbS CQDs and Bi_2Te_3 material results in a broadband response of up to 1050 nm that is beyond the absorption range of PbS CQDs. In addition, the well-designed energy band alignment of AZO/Bi_2Te_3/PbS CQDs hybrid structure would accelerate carrier transmission, hence enhancing the performance of the device between visible light and near infrared with ultra-high responsivity and detectivity

of 161 A/W and 3.2×10^{13} Jones at 1050 nm, respectively. The hybrid structure has great potential in the development of next generation optoelectronic devices.

Data availability

Data will be made available on request.

CRediT authorship contribution statement

Lijing Yu: Methodology, Investigation, Writing – original draft. **Pin Tian:** Methodology. **Libin Tang:** Methodology, Funding acquisition, Writing – review & editing. **Qun Hao:** Writing – review & editing. **Kar Seng Teng:** Writing – review & editing. **Hefu Zhong:** Data curation. **Wenbin Zuo:** Data curation. **Yulong Ji:** . **Hongfu Li:** . **Zhihua Li:** . **Qi Ma:** . **Min Yang:** . **Lianjie Yu:** .

Data availability

The data that has been used is confidential.

Declaration of Competing Interest

The authors declare that they have no known competing financial interests or personal relationships that could have appeared to influence the work reported in this paper.

Appendix A. Supplementary material

Supplementary data to this article can be found online at https://doi.org/10.1016/j.matdes.2023.111934.

References

[1] Y. Yu, Y. Zhang, Z. Zhang, H. Zhang, X. Song, M. Cao, et al., Broadband Phototransistor Based on CH$_3$NH$_3$PbI$_3$ Perovskite and PbSe Quantum Dot Heterojunction, J. Phys. Chem. Lett. 8 (2017) 445–451.

[2] J. Yao, G. Yang, 2D material broadband photodetectors, Nanoscale 12 (2020) 454–476.

[3] K. Gong, L. Li, W. Yu, H. Mu, J. Yuan, R. Hao, et al., High detectivity and fast response avalanche photodetector based on GaSe/PtSe$_2$ p–n junction, Mater. Des. 228 (2023) 111848.

[4] X. Hu, X. Zhang, L. Liang, J. Bao, S. Li, W. Yang, et al., High-Performance Flexible Broadband Photodetector Based on Organolead Halide Perovskite, Adv. Funct. Mater. 24 (2014) 7373–7380.

[5] S.B. Brichkin, V.F. Razumov, Colloidal quantum dots: synthesis, properties and applications, Russ. Chem. Rev. 85 (2016) 1297–1312.

[6] Z. Ren, J. Sun, H. Li, P. Mao, Y. Wei, X. Zhong, et al., Bilayer PbS Quantum Dots for High-Performance Photodetectors, Adv. Mater. 29 (2017).

[7] J. Yang, H. Hu, Y. Lv, M. Yuan, B. Wang, Z. He, et al., Ligand-Engineered HgTe Colloidal Quantum Dot Solids for Infrared Photodetectors, Nano Lett. 22 (2022) 3465–3472.

[8] L. Liu, A. Najar, K. Wang, M. Du, S.F. Liu, Perovskite Quantum Dots in Solar Cells, Adv. Sci. 9 (2022) e2104577.

[9] J. Deng, H. Wang, J. Xun, J. Wang, X. Yang, W. Shen, et al., Room-temperature synthesis of excellent-performance CsPb$_{1-x}$Sn$_x$Br 3 perovskite quantum dots and application in light emitting diodes, Mater. Des. 185 (2020) 108246.

[10] Z. Mamiyev, N.O. Balayeva, PbS nanostructures: A review of recent advances, Mater. Today Sustain. 21 (2023) 100305.

[11] M.S. Neo, N. Venkatram, G.S. Li, W.S. Chin, J. Wei, Size-Dependent Optical Nonlinearities and Scattering Properties of PbS Nanoparticles, J. Phys. Chem. C 113 (2009) 19055–19060.

[12] J. Chang, E.R. Waclawik, Colloidal semiconductor nanocrystals: controlled synthesis and surface chemistry in organic media, RSC Adv. 4 (2014) 23505–23527.

[13] J.W. Lee, D.Y. Kim, S. Baek, H. Yu, F. So, Inorganic UV-Visible-SWIR Broadband Photodetector Based on Monodisperse PbS Nanocrystals, Small 12 (2016) 1328–1333.

[14] R. Saran, R.J. Curry, Lead sulphide nanocrystal photodetector technologies, Nat. Photonics 10 (2016) 81–92.

[15] H. Choi, J.H. Ko, Y.H. Kim, S. Jeong, Steric-hindrance-driven shape transition in PbS quantum dots: understanding size-dependent stability, J. Am. Chem. Soc. 135 (2013) 5278–5281.

[16] M. Albaladejo-Siguan, E.C. Baird, D. Becker-Koch, Y. Li, A.L. Rogach, Y. Vaynzof, Stability of Quantum Dot Solar Cells: A Matter of (Life)Time, Adv. Energy Mater. 11 (2021) 2003457.

[17] L. Yu, P. Tian, L. Tang, Q. Hao, K.S. Teng, H. Zhong, et al., Fast-Response Photodetector Based on Hybrid Bi$_2$Te$_3$/PbS Colloidal Quantum Dots, Nanomaterials 12 (2022).

[18] M.A. Hines, G.D. Scholes, Colloidal PbS Nanocrystals with Size-Tunable Near-Infrared Emission: Observation of Post-Synthesis Self-Narrowing of the Particle Size Distribution, Adv. Mater. 15 (2003) 1844–1849.

[19] W. Chen, H. Tang, Y. Chen, J.E. Heger, N. Li, L.P. Kreuzer, et al., Spray-deposited PbS colloidal quantum dot solid for near-infrared photodetectors, Nano Energy 78 (2020) 105254.

[20] I. Moreels, K. Lambert, D. Smeets, D. De Muynck, T. Nollet, J.C. Martins, et al., Size-Dependent Optical Properties of Colloidal PbS Quantum Dots, ACS Nano 3 (2009) 3023–3030.

[21] Z.Q. Mamiyev, N.O. Balayeva, Preparation and optical studies of PbS nanoparticles, Opt. Mater. 46 (2015) 522–525.

[22] M. Yuan, D. Zhitomirsky, V. Adinolfi, O. Voznyy, K.W. Kemp, Z. Ning, et al., Doping control via molecularly engineered surface ligand coordination, Adv. Mater. 25 (2013) 5586–5592.

[23] L. Hu, D.-B. Li, L. Gao, H. Tan, C. Chen, K. Li, et al., Graphene Doping Improved Device Performance of ZnMgO/PbS Colloidal Quantum Dot Photovoltaics, Adv. Funct. Mater. 26 (2016) 1899–1907.

[24] G. Yang, Y. Zhu, J. Huang, X. Xu, S. Cui, Z. Lu, Hole transport layer selection toward efficient colloidal PbS quantum dot solar cells, Opt. Express 27 (2019) A1338–A1349.

[25] J. Tang, L. Brzozowski, D.A.R. Barkhouse, X. Wang, R. Debnath, R. Wolowiec, et al., Quantum Dot Photovoltaics in the Extreme Quantum Confinement Regime: The Surface-Chemical Origins of Exceptional Air- and Light-Stability, ACS Nano 4 (2010) 869–878.

[26] M.-W. Jeong, S. Na, S. Shin, H.-B. Park, H.-J. Lee, Y.-C. Joo, Thermomechanical In Situ Monitoring of Bi$_2$Te$_3$ Thin Film and Its Relationship with Microstructure and Thermoelectric Performances, Electron. Mater. Lett. 14 (2018) 426–431.

[27] M. Ahmad, K. Agarwal, B.R. Mehta, An anomalously high Seebeck coefficient and power factor in ultrathin Bi$_2$Te$_3$ film: Spin–orbit interaction, J. Appl. Phys. 128 (2020) 035108.

[28] B.N. Pal, I. Robel, A. Mohite, R. Laocharoensuk, D.J. Werder, V.I. Klimov, High-Sensitivity p-n Junction Photodiodes Based on PbS Nanocrystal Quantum Dots, Adv. Funct. Mater. 22 (2012) 1741–1748.

[29] J. Tang, E.H. Sargent, Infrared colloidal quantum dots for photovoltaics: fundamentals and recent progress, Adv. Mater. 23 (2011) 12–29.

[30] M.J. Grotevent, C.U. Hail, S. Yakunin, D.N. Dirin, K. Thodkar, G. Borin Barin, et al., Nanoprinted Quantum Dot-Graphene Photodetectors, Adv. Opt. Mater. 7 (2019) 1900019.

[31] D. Kufer, I. Nikitskiy, T. Lasanta, G. Navickaite, F.H. Koppens, G. Konstantatos, Hybrid 2D–0D MoS$_2$ -PbS quantum dot photodetectors, Adv. Mater. 27 (2015) 176–180.

[32] L. Gao, C. Chen, K. Zeng, C. Ge, D. Yang, H. Song, et al., Broadband, sensitive and spectrally distinctive SnS$_2$ nanosheet/PbS colloidal quantum dot hybrid photodetector, Light Sci. Appl. 5 (2016) e16126.

[33] S. Masala, V. Adinolfi, J.P. Sun, S. Del Gobbo, O. Voznyy, I.J. Kramer, et al., The Silicon: Colloidal Quantum Dot Heterojunction, Adv. Mater. 27 (2015) 7445–7450.

[34] C. Hu, D. Dong, X. Yang, K. Qiao, D. Yang, H. Deng, et al., Synergistic Effect of Hybrid PbS Quantum Dots/2D-WSe$_2$ Toward High Performance and Broadband Phototransistors, Adv. Funct. Mater. 27 (2017) 1603605.

[35] K. Qiao, H. Deng, X. Yang, D. Dong, M. Li, L. Hu, et al., Spectra-selective PbS quantum dot infrared photodetectors, Nanoscale 8 (2016) 7137–7143.

[36] L. Mi, Y. Chang, Y. Zhang, E. Xu, Y. Jiang, Hybrid perovskite exchange of PbS quantum dots for fast and high-detectivity visible–near-infrared photodetectors, J. Mater. Chem. C 8 (2020) 7812–7819.

[37] Z. Sun, Z. Liu, J. Li, G.-A. Tai, S.-P. Lau, F. Yan, Infrared Photodetectors Based on CVD-Grown Graphene and PbS Quantum Dots with Ultrahigh Responsivity, Adv. Mater. 24 (2012) 5878–5883.

[38] P. Liu, B. Liu, Y. Zhang, Z. Jiang, H. Zhao, Highly efficient optoelectronic devices based on colloidal heterostructured quantum dots, APL Mater. 9 (2021) 050701.